RSC Advances

PAPER

View Article Online
View Journal | View Issue

Cite this: *RSC Adv.*, 2025, **15**, 33297

Promoting the viability of soybean biodiesel by mitigating its oxidative effects on austenitic stainless steel using a natural additive of spent coffee grounds

Maha El Hawary, [a] Othon S. Campos,[b] Younes Kerroum, [a] Abdelkbir Bellaouchou, [a] Hatem M. A. Amin *[cd] and Maria Boudalia [a]

This work demonstrates the recycling potential of a hydroalcoholic extract of spent coffee waste (HECG) as an environmentally friendly additive to soybean cooking oil (SWCO) biodiesel, alleviating its corrosive impacts on a Cr-rich stainless-steel alloy. The extract is efficiently produced using the Soxhlet extraction method, and its chemical profile is analyzed using GC-MS and FTIR. Furthermore, the anticorrosive properties of HECG are thoroughly evaluated using gravimetry, potentiodynamic polarization, and electrochemical impedance spectroscopy (EIS). The HECG additive shows excellent inhibitory efficacy (94%) on 307 L stainless steel. The polarization results underline the mixed inhibitory character of HECG. The metal surface is primarily protected against biodiesel-induced corrosion through adsorption of additive molecules onto it. Additionally, SEM-EDX and XRD techniques are used to evaluate the microstructure, crystal structure, and composition of the surface and formed products after immersion in this biodiesel. The results showcase the additional protection of the 307 L sample via creating a passive oxide film (CrO_{23}, FeO_{23}, FeOOH) on the metal surface, thus boosting its corrosion resistance. Importantly, DFT and Fukui function simulations identify the electrophilic and nucleophilic sites at the β-turmerone molecule, the major component of the extract, and reveal intrinsic retro donations in both ways – additive to metal and/or metal to additive.

Received 8th July 2025
Accepted 28th August 2025

DOI: 10.1039/d5ra04888e

rsc.li/rsc-advances

1. Introduction

The growth of generating biofuels from waste cooking oil constitutes a significant technical advancement, thus providing a sustainable alternative to conventional petroleum-based fuels.[1] As a reflection of its significance, 43 billion Liters of biodiesel were produced worldwide in 2021 and its production is expected to rise in the coming decade.[2] Biofuels are typically produced from renewable biomass such as soybean, cottonseed, animal fat, and residual oil and are used in transportation, thus offering an environmentally friendly and cleaner alternative to traditional fuel.[3] Among others, waste cooking oil is considered the most viable source for biodiesel production because of its economic benefit. It is usually discarded as waste in vast amounts from restaurants, industries, households, and others. Biodiesel, in particular, stands out for its biodegradability, low toxicity, flexible production from various biosources, and reduced emissions of pollutants.[4,5] It also has advantages over petroleum diesel including better engine performance, low volatility, higher flash point, and easier transportation and storage.[6] However, biodiesel has more corrosive effects than petroleum diesel on various metal surfaces.[7] Results showed that the corrosion rate depends on the metal, with stainless steel the most resistant metallic material compared to copper and aluminum. According to Nernst's hypothesis, metals have a natural tendency to corrode in solution. Regardless, corrosion levels are affected by external variables such as moisture content, acidity, temperature, impurities, dissolved oxygen, microbial activity, contact with other materials, and flow conditions, including the presence of biodiesel.[8] Metal corrosion is a crucial issue in vehicles as many parts of the engine are made of metals such as copper, aluminum, stainless steel, and their alloys. These metallic parts are susceptible to corrosion at various rates, leading to considerable damage. Such corrosion has an impact on engine performance, durability, and safety, thus emphasizing the importance of appropriate corrosion control measures, particularly in biodiesel-powered engines.[9]

[a]*Laboratory of Materials, Nanotechnology and Environment, Faculty of Sciences, Mohammed V University in Rabat, P.O. Box 1014, 10000 Rabat, Morocco*

[b]*Department of Chemistry and Physics, Federal University of Espírito Santo, 29500-000 Alegre-ES, Brazil*

[c]*Chemistry Department, Faculty of Science, Cairo University, 12613 Giza, Egypt. E-mail: hatem.amin@uni-due.de*

[d]*Faculty of Chemistry, University of Duisburg-Essen, 45141 Essen, Germany*

The challenge worsens in biodiesel engines because of the fuel's strong affinity to water, which causes hydrolysis and the formation of corrosive byproducts such as fatty acids and glycerol. Moreover, incomplete transesterification and residues such as water, free glycerol, methanol, and fatty acids can contribute to corrosion.[10] Furthermore, biodiesel's lubricating characteristics and trace metals might hasten metal deterioration.[11] Hence, highlighting the importance and necessity of effective corrosion control strategies is crucial to safeguarding engine components and maintaining peak performance.[12]

Two main strategies can be used to mitigate the corrosion in biodiesel, namely the use of corrosion resistance alloys or the addition of corrosion inhibitors. Although corrosion-resistant materials can significantly reduce the negative effects of corrosive species, their high cost and special manufacturing requirements make inexpensive metallic materials in combination with effective corrosion inhibitors the preferred choice in many industrial applications. In this context, the corrosion cost index serves as a dependable measure of the effectiveness of prevention and protection methods in mitigating the expenses associated with corrosion-induced deterioration.[13] Several means are employed for corrosion protection: either protection using coatings (organic or inorganic) or inhibitors.[14] These approaches increase the metal's corrosion resistance by establishing a shield between the substrate and the environment.[15] The application of corrosion inhibitors has proven to be one of the most effective strategies for mitigating corrosion across a wide range of materials.[16] However, most organic and inorganic inhibitors involve hazardous materials and exhaustive synthetic routes.[17,18] Alternatively, eco-friendly inhibitors are currently attracting great interest in corrosion protection due to their safety, biodegradability, environmental acceptability, and renewable nature.[19–21] Biomaterials are rich in phytochemicals that can effectively adsorb onto the metal surface, forming a protective layer against the attack of biodiesel components.

Almost all organic molecules in extracts tend to adhere to metal surfaces. When the corrosion inhibitor's effect is specifically targeted, the most desirable properties are those related to the metal's electrostatic attraction to the inhibitor's charged molecules, the double-, triple-, or single–electron interaction of N, S, P, or O with the metal's vacant d-orbitals, or a combination of some of the aforementioned mechanisms.[22] Therefore, the emphasis on resources for environmentally friendly natural products and low-cost compounds as metal corrosion inhibitors has grown in recent decades.[23] For example, rice bran oil, a byproduct of rice processing, contains bioactive compounds such as oryzanol and tocopherols, which minimize corrosion by creating a thin protective layer and thus decreasing the availability of aggressive ions.[24] Although extracts from biowaste are largely investigated as green inhibitors for metallic surfaces in acidic and saline environments, research on their effectiveness in biodiesel is limited. Only a few examples are reported on the use of natural extracts as anticorrosion additives in biofuels.[25,26] For example, cardanol extract from cashew nutshell liquid demonstrated an increased inhibition efficiency (93.2%) for aluminum alloy in soybean biodiesel.[25,26] Recently, *Thymus vulgaris* extract showed a significant decrease in aluminum corrosion in 20% biodiesel-80% diesel blend.[27] *Terminalia catappa* leaf extract has also effectively reduced the corrosion of carbon steel and zinc, however its corrosion inhibition efficiency was limited (78% at room temperature and 8% at 60 °C for zinc).[25,26] Nevertheless, these biowaste-derived inhibitors not only effectively combat corrosion but also promote sustainability by utilizing waste materials, highlighting their potential in biodiesel applications. Thus, investigating more efficient inhibitors in biodiesels is of scientific and economic interest.

Additionally, there is enormous potential in waste food valorisation as a sustainable option for synthetic inhibitors due to the ability to generate economic benefits from waste materials. One type of residual food that several researchers have attempted to recover is waste coffee grounds since they are rich in dietary fibre, protein, essential amino acids, and sugar.[28] Spent coffee bean extracts showed remarkable inhibitory effectiveness for Cu in a 3% NaCl solution and for carbon steel in acidic media.[29,30] Moreover, recycling organic waste such as coffee grounds would contribute to the transition from a linear economy to a circular bioeconomy, which would bring ecological and economic benefits.

While the valorization of spent coffee grounds (SCG) offers clear environmental and economic benefits, its large-scale deployment is influenced by cost-related factors including drying energy (as SCG typical exits the brewing with 55–70% moisture), thermal duty and solvent make-up and recovery. Nevertheless, the simplicity of the Soxhlet extraction procedure would facilitate its upscaling. Furthermore, the economic benefits may need to be balanced not only by the extraction cost but also by co-product revenues, as well as government incentives for renewable resources, to play a significant role in determining profitability. Finally, the presence of natural antioxidants in SCG oil supports the compatibility of this oil-soluble additive with the standard additive dosing infrastructure for biodiesel, limiting additional capital requirements. Nevertheless, the overall feasibility depends mainly on minimizing drying and distillation loads and securing reliable SCG logistics on a scale. To our knowledge, its use as an additive in biodiesel for stainless steel protection has not been reported yet.

In the present work, the potential of the hydroalcoholic extract of spent coffee grounds (HECG) was evaluated as an additive to soybean oil biodiesel to control the oxidation of stainless steel (307 L S-steel). This approach aims to boost the viability of soybean biodiesel. The inhibition properties were investigated using both gravimetric and electrochemical (potentiodynamic polarization and EIS) methods. Furthermore, the study was extended to explore how effectively this additive prevents the damage of 307 L S-steel at various temperatures, allowing determination of thermodynamic parameters. Additionally, the nature of the interfacial processes, passivation products, and the inhibition mechanism were elucidated based on microscopic (SEM-EDX) and spectroscopic (FTIR, UV-Vis) data. Moreover, the crystalline structure of the samples with and without the HECG additive was thoroughly studied using XRD. Importantly, the nature of the interactions between the additive inhibitor and the steel surface as well as the underlying

protection mechanism were unraveled by DFT simulations and Fukui functions, which well supported the electrochemical and spectroscopic results. Our approach demonstrates the potential of recycling waste coffee grounds as an additive to increasing the sustainability of soybean biodiesel.

2. Experimental

2.1. Materials

The corrosion tests were performed on the austenitic stainless steel 307 L (307 L S-steel) containing 19% Cr, 9% Ni, 2.72% Mo, balance Fe by weight. The stainless-steel coupons (1 cm^2 exposed surface area) were polished using abrasive papers with grit sizes of 120, 400, 800, 1000, and 1200, in an ascending order. After polishing, the electrodes were rinsed with distilled water and cleaned with acetone before drying in air.

2.2. Biodiesel synthesis and physicochemical characterization

The soybean waste cooking oil (SWCO) and methanol (99%) used in the studied biodiesel were processed with the help of a heterogeneous acid catalyst. Details on the biodiesel synthesis and its conditions are reported in our previous work[31] and summarized in the SI file.

The physicochemical characteristics of the biodiesel were determined following the European (EN-14214) and American (ASTM D-6751-11b) standards, including viscosity, density, acid number, flash point, ester content, cold filtration test, sulfur content, and lubricity.[32,33]

2.3. Preparation and characterization of coffee grounds extract as an additive

2.3.1. Sample collection and coffee grounds extraction. Fig. 1 shows the detailed steps of the extraction procedure of coffee grounds extract. Details of the procedure are given in the SI. The leftover coffee grounds were first dried to remove moisture. Afterwards, a hydroalcoholic extract was prepared using the Soxhlet extraction method. The extraction efficiency was calculated as follows:

$$Y = \frac{m_{ext}}{m_{sample}} \times 100 \quad (1)$$

where, Y is the yield in percentage, m_{ext} is the mass of the extract after evaporation of the solvent in grams and m_{sample} represents the dry mass of the sample before extraction. The extraction yield was estimated to be about 12%.

2.3.2. Characterization methods of HECG extract. GC-MS analysis was conducted to identify the chemical composition of the spent coffee grounds extract using a PerkinElmer Auto System XL GC (Waltham, MA, USA). The sample was also characterized using a single reflection Pro One attenuated total reflectance (ATR)-FT/IR-Jasco 4600 spectrometers with a monolithic diamond crystal. Details of these analyses are presented in the SI.

2.4. Corrosion assessment methods

2.4.1. Gravimetric method (weight loss). For the present study, specimens were prepared in closed glass bottles holding 50 mL of the electrolyte with different concentrations of HECG extract. The experiments were conducted with varied inhibitor concentrations. After immersion for 1128 h, the samples were removed and thoroughly rinsed with distilled water and acetone before being dried and reweighed. The tests were performed following ASTM G 31-72.[34] The corrosion rate C_R is determined according to the following eqn (2):

$$C_R = \frac{W}{A \times t \times \rho} \quad (2)$$

with W representing the weight loss in g, A is the surface area exposed in cm^2, ρ is the metal density (g cm^{-3}), and t is the time

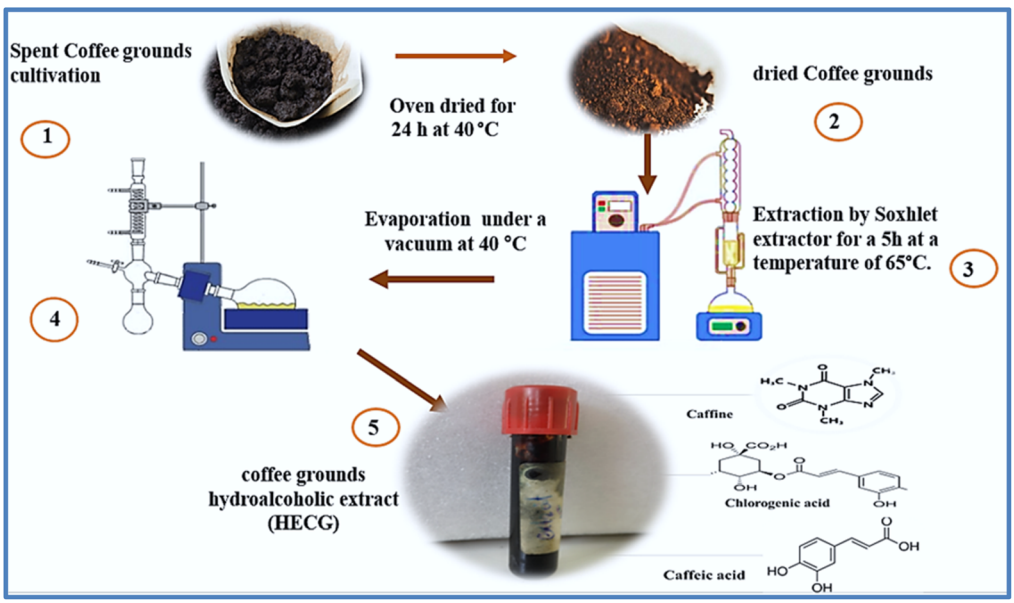

Fig. 1 Schematic of the extraction procedure of coffee grounds hydroalcoholic extract.

the samples spent immersed in the tested solution, usually expressed in hours. Based on the corrosion rates C_R (in the blank) and $C_{R\text{-inh}}$ (in the presence of inhibitor), the inhibition efficiency ($\eta_{WL}\%$) was calculated as follows:

$$\eta_{WL}\% = \frac{C_R - C_{R\text{-inh}}}{C_R} \times 100 \quad (3)$$

2.4.2. Electrochemical measurements. Electrochemical measurements were conducted using a three-electrode configuration. The potentiodynamic polarization curves were recorded and the Tafel tangents of anodic and cathodic lines were used to obtain i_{corr} (in the absence of HECG) and i_{corr}^{inh} (in the presence of HECG), from which the PDP inhibition efficiency (%) was calculated using eqn (4):

$$\eta_{PDP}\% = \frac{i_{corr} - i_{corr}^{inh}}{i_{corr}} \times 100 \quad (4)$$

Furthermore, the electrochemical impedance spectroscopy (EIS) was recorded and the polarization resistance in the absence (R_P°) and presence (R_p) of the inhibitor were calculated from the charge transfer resistance R_{ct} and the film resistance R_f created by the corrosion products and passive film using eqn (5). These EIS data were then used to determine the effectiveness of the examined molecule's inhibition using eqn (6).

$$R_p = R_{ct} + R_f \quad (5)$$

$$\eta_{EIS}\% = \frac{R_P - R_P^\circ}{R_P} \times 100 \quad (6)$$

2.5. Surface and spectroscopic characterization of the electrode surface

To evaluate the impact of the chemical composition of corrosion products formed on 307 L S-steel surface in biodiesel, UV-Vis-NIR spectra were recorded in the range from 190 to 1000 nm using a Jasco Model V670 spectrophotometer. The surface morphology and the composition of corrosion products were investigated using SEM (JEOL JFC-2300HR SEM) that was equipped with an EDX unit. XRD diffractograms of the specimen surface were captured using a Shimadzu diffractometer with Cu Kα radiation (Cu = 1.5406 Å) and a 30 kV/10 mA step.

2.6. DFT calculations

DFT calculations were performed on β-turmerone as the major constituent of the coffee extract based on the chemical composition. First, the β-turmerone molecule was drawn in Avogadro version 1.2[35] and the *xyz* file was optimized using the GFN2-XTB package.[36] Afterward, the *xyz* files were submitted to a DFT computation using the ORCA 5.0.4 package[37] in a Linux-based environment with optimized hardware. The calculation setup ran over Minnesota 06-2X[38] functional along People's 6–311 + g (d, p) orbital basis set,[39] and RIJ-COSX coulombic integration method for calculation optimization. The orbital files were taken from conventional output files using "orca_plot" software for exporting into cube files to be opened in Chemcraft version 1.8.[40] All DFT calculations for optimization of the inhibitor molecule were in a global minimum since the theoretical IR spectra of those compounds showed no negative frequencies. The following important molecular descriptors were calculated using the energy data from calculated output files, using the following eqn [41]

$$IE = -E_{HOMO} \quad (7)$$

$$EA = -E_{LUMO} \quad (8)$$

$$\omega^+ = \frac{(EI + 3 \times AE)^2}{16(EI - AE)} \quad (9)$$

$$\omega^- = \frac{(3 \times EI + AE)^2}{16(EI - AE)} \quad (10)$$

$$\eta = \frac{EI - AE}{2} \quad (11)$$

$$\chi = -\frac{AE + EI}{2} \quad (12)$$

$$\Delta\omega = \omega^+ - \omega^- \quad (13)$$

where, IE and EA are the ionization energy and electron affinity of geometrized β-turmerone molecules, respectively. ω^+ and ω^- stand for electro-reception and electro-donation, respectively, and $\Delta\omega$ is the liquid electrophilicity. Lastly, η and χ are the chemical hardness and electronegativity, respectively. An important parameter that helps to identify the capability of an inhibitor to interact with the metal surface is the electron transfer number between the inhibitor molecule and electrode surface (ΔN). This parameter was calculated from molecular descriptors of the frontier molecular orbitals (FMO) based on Pearson's HSAB theory[42–45] as follows:

$$\Delta N = \frac{\varphi - \chi_{inh}}{2\eta_{inh}} \quad (14)$$

where, φ is the work function of the metal from an electrode, χ_{inh} is the inhibitor molecule's electronegativity and η_{inh} is the inhibitor's chemical hardness. Considering that the steel electrode contains polycrystalline iron, the work function was 4.70 eV.[46] Furthermore, Fukui function analysis was conducted using the calculated wavefunctions of the prior optimization files, and the output files were submitted to the following operations in Chemcraft [47]

$$\rho^+ = \rho_{N+1} - \rho_N \quad (15)$$

$$\rho^- = \rho_N - \rho_{N-1} \quad (16)$$

$$\rho^\cdot = \frac{1}{2}(\rho_{N+1} - \rho_{N-1}) \quad (17)$$

where ρ^+, ρ^+, and $\rho^\cdot$ are the nucleophilic, electrophilic, and radical wavefunctions over the β-turmerone molecule, respectively, and ρ_{N+1} and ρ_{N-1} are the anionic and cationic

wavefunctions related to the ρ_N neutral wavefunction, respectively. These Fukui surfaces show how the β-turmerone will undergo nucleophilic, electrophilic, and radical reactions in this system.

3. Results and discussion

3.1. Physicochemical properties of SWCO

The physicochemical characteristics of soybean biodiesel are listed in Table S1. During these tests, water flowed from a thermostat to maintain a consistent operational temperature during all measurements conducted in a double-walled cell with a glass plate covering it. Based on the results obtained, the SWCO biodiesel quality is in full accordance with ASTM standards.[48,49]

3.2. Identification of HECG chemical profile using GC-MS

GC-MS analysis was initially applied to identify the chemical profile of the coffee extract. The GC-MS chromatogram reveals the presence of volatile and bioactive compounds in HECG with various retention times, as shown in Fig. S1. Table 1 lists the respective chemical compositions of HECG. 13 compounds were identified, and the main components are β-Turmerone (32.49%), nitrogenous compounds such as trigonelline (18.0%), polyphenolic compounds such as chlorogenic acid (8.68%), caffeic acid and caffeine. According to the literature, extracts from in coffee grounds is high in these compounds.[50] These compounds are rich in oxygen-containing functional groups that can bind to the metal surface and thus promote their adsorption. Thus, the main phenolic compound found in our extract was β-Turmerone which is expected to contribute to corrosion inhibition.

3.3. FT-IR spectroscopic analysis of the extract additive

The functional groups and spectral ranges characteristic of the coffee brand were identified using FTIR analysis as shown in Fig. 2. The detection of a large band at 3334 cm^{-1} is mainly attributed to O–H stretching vibration. Possible inter and intramolecular hydrogen interactions can occur between OH functional groups in compounds such as phenols and carboxylic acids found in pectin, cellulose, and lignin. The band between 2882–2829 cm^{-1} is attributed to the asymmetric stretching of C–H bonds of the methylamine ($N–CH_3$), predominantly in the caffeine molecule. This can be effectively exploited in the quantitative detection of caffeine content.[51]

Furthermore, the peak observed in the range of 1700–1654 cm^{-1} in the IR spectrum of methanolic coffee extract is primarily associated with the carbonyl (C=O) stretching vibrations of ester groups in chlorogenic acids. These compounds formed from the esterification of caffeic acid and quinic acid exhibit strong absorption in this region due to their carbonyl functionalities.

While caffeine also contains carbonyl groups that may contribute to this peak, the predominant attribute in this range is to the carbonyl groups in chlorogenic acids, reflecting their significant presence and interaction in the coffee extract. The C=O bond is stretched similarly to the peak at 1712 cm^{-1} in the presence of lipids and aliphatic esters. The large band between 1135 and 952 cm^{-1} results from C–O stretching vibration in C–O–H bonds such as glycosidic bonds and is associated with galactomannan polysaccharides' sugars.[52]

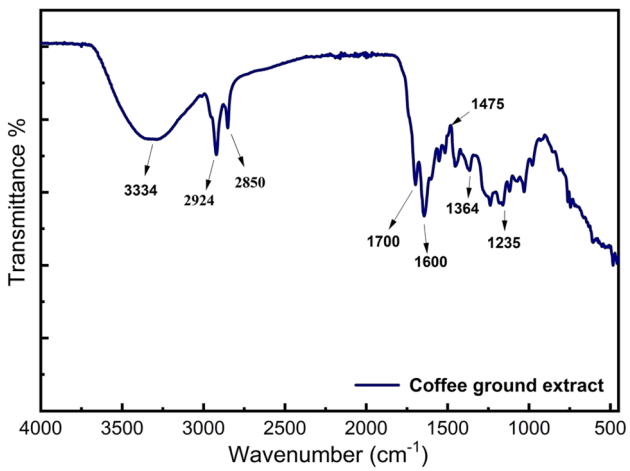

Fig. 2 FTIR spectrum of the spent coffee grounds extract.

Table 1 GC-MS analysis of components found in the HECG extract

Retention time (min)	%	Name of compounds	Formula	MW (g mol^{-1})
10.5	32.49	β-Turmerone	$C_{15}H_{22}O$	218.0
5.4	8.68	Chlorogenic acid	$C_{16}H_{18}O_9$	354.3
5.3	2.25	Caffeic acid	$C_9H_8O_4$	180.2
3.5	5.69	2-Amino-4,6-dimethylpyrimidine	$C_6H_9N_3$	123.2
1.8	7.64	4-Hydroxy-5-oxohexanoic acid	$C_6H_{10}O_4$	146.1
9.7	1.67	4-Methyl-dibenzothiophene	$C_{13}H_{10}S$	198.0
11.4	18.01	Trigonelline	$C_7H_7NO_2$	140.3
1.0	3.92	4-Vinyl-2-methoxy phenol	$C_9H_{10}O_2$	150.3
1.4	4.37	3-Pyridinol	C_5H_5NO	95.0
2.9	3.24	5-Methylfurfural	$C_6H_6O_2$	110.1
3.9	2.69	3″-Hydroxy-geranylhydroquinone	$C_{16}H_{22}O_3$	262.3
6.9	3.08	1-Methyl-4-prop-1-en-2-ylcyclohexene	$C_{10}H_{18}$	138.3
6.3	7.64	Caffeine	$C_8H_{10}N_4O_2$	194.2

Table 2 Corrosion rate results and inhibition efficiency from weight loss measurements after 1128 h immersion at 303 K in biodiesel containing various concentrations of HECG

Conc. (ppm)	C_R (mg cm^{-2} h^{-1})	η_{WL}%
0 (blank)	113.6	—
500	24.2	78.7
750	17.4	84.6
1500	3.4	97.0

3.4. Evaluation of the corrosion resistance in biodiesel oil

3.4.1. Weight loss assay. Initially, the weight loss method was utilized as the simplest tool to determine the effectiveness of the HECG additive in SWCO biodiesel and estimate the corrosion rate of the 307 L S-steel specimen. The weight loss of all samples was measured before and after 1128 h of immersion in a SWCO biodiesel bath containing different concentrations of HECG at a controlled temperature (303 K). As summarized in Table 2, the corrosion rate (C_R) of 307 L S-steel decreases from 113.6 to 3.4 mg cm^{-2} h^{-1} after the addition of the 1500 ppm inhibitor. The inhibition efficiency η_{WL} (%) increases from 78.7% to 97.0% as the concentration increases from 500 to 1500 ppm. As the inhibitor concentration increases, more molecules of the inhibitor additive adhere to the 307 L S-steel surface, blocking more active sites for corrosion and consequently effectively halting the mass loss.[53]

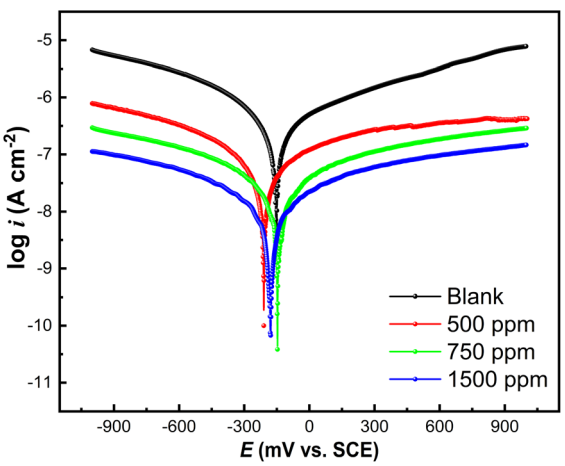

Fig. 3 Polarization curves at 307 L S-steel in SWCO biodiesel without and with various concentrations of HECG.

3.4.2. Electrochemical evaluation of HECG additive on steel oxidation

3.4.2.1. Potentiodynamic polarization (PDP). Potentiodynamic polarization measurements were then conducted to gain quantitative information on the efficiency and kinetics of the HECG additive. The polarization curves were recorded across both the cathodic and anodic potential ranges. Fig. 3 depicts the effect of different HECG concentrations in SWCO biodiesel on the potentiodynamic polarization curves of 307 L S-steel. Table 3 presents the obtained electrochemical parameters including corrosion potential (E_{corr}), current density (i_{corr}), anodic and cathodic Tafel slopes (β), and inhibition efficiency (%). As shown in Table 3, i_{corr} markedly declined from 201 nA cm^{-2} to 13 nA cm^{-2} after the addition of 1500 ppm HECG extract, proving its effective inhibitive effect. Additionally, it is found that increasing the concentration of HECG diminishes both anodic and cathodic current densities. The variation in E_{corr} values could be due to the adsorption of organic molecules from the extract onto the electrode surface, which can alter the active site. This adsorption might be the consequence of the chemical inhibitor's contact with the steel surface, boosting passive film development, or the synergistic action of several organic corrosion inhibitors.

The polarization data showed that HECG is effective as a corrosion inhibitor, exhibiting distinct anodic and cathodic reaction kinetics compared to blank solutions. The polarization measurements indicate that the corrosion potential shifts in two directions when HECG is present, suggesting that it functions as a mixed-type inhibitor.[54] This shift signifies that HECG can effectively hinder both anodic and cathodic processes, enhancing overall corrosion protection in various environments.[55] Based on these findings, we propose that HECG performs by inhibiting electrochemical anodic and cathodic active sites on the SS surface and producing a protective layer.[16]

In accordance with Table 3, as the concentration of HECG increased, the corrosion current density (i_{corr}) decreased. The adsorption of HECG molecules on the 307 L S-steel surface slowed down the rate of electrochemical reaction. Furthermore, the inhibitory efficiency (η_{PDP}%) has increased with increasing the HECG inhibitor concentration, reaching a maximum of 93.5% for 1500 ppm of HECG. These results agree with the weight loss data, demonstrating that increasing the inhibitor concentration causes more adsorption of the inhibitor molecules and, as a result, a reduction in the surface sites accessible for corrosion.

3.4.2.2. Electrochemical impedance spectroscopy (EIS). EIS was used to further examine the corrosion inhibition abilities of

Table 3 Electrochemical parameters obtained from the polarization curves at 307 L S-steel in SWCO biodiesel with various concentrations of HECG

Conc. (ppm)	$-E_{corr}$ (mV *vs.* SCE)	i_{corr} (nA cm^{-2})	β_a (mV dec^{-1})	β_c (mV dec^{-1})	η_{PDP}%
Blank	154 ± 2	201 ± 5	282.0	324.8	—
500	210 ± 5	43 ± 2	440.4	303.7	78.6
750	147 ± 2	30 ± 1	416.8	389.7	85.0
1500	180 ± 4	13 ± 0.3	128.3	130.1	93.5

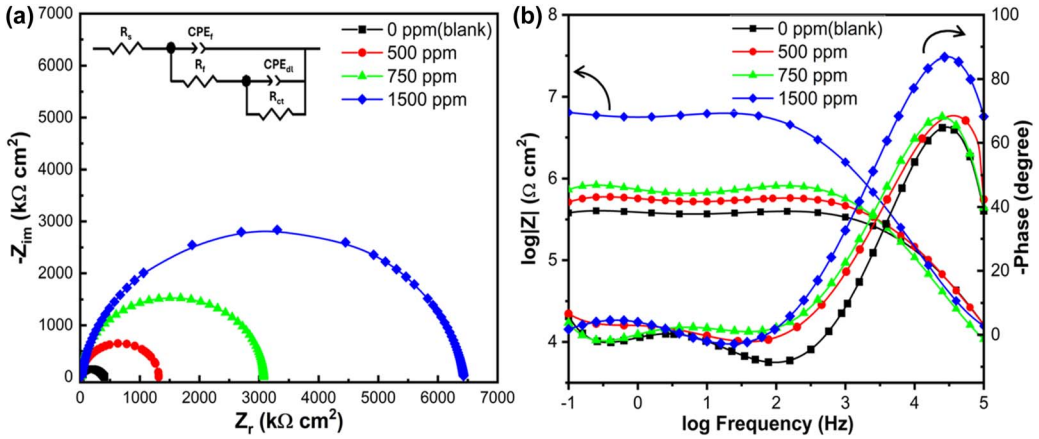

Fig. 4 EIS Nyquist (a) and Bode (b) plots obtained at 307 L S-steel in SWCO biodiesel with varying HECG concentrations.

HECG on S-steel and gain important insights into the charge transfer processes at the steel interface.[14,56,57] Nyquist plots obtained the OCP for 307 L S-steel in SWCO biodiesel at various HECG concentrations are shown in Fig. 4.

Nyquist plots (Fig. 4a) revealed two depressed overlapped semicircles with centers below the real axis, indicating the presence of two capacitive loops. This observation aligns with the Bode plots (Fig. 4b) where two typical peaks were observed, indicating the presence of two-time constants. This finding indicates that the charge transfer primarily regulates the electrochemical processes at the interface. Furthermore, the diameter of the observed arc significantly increases with the addition of HECG compared to the blank case, proving an increased surface resistance. This can be explained by the formation of an inhibitor layer and a passive oxide film on the steel surface, thus increasing the resistance and consequently boosting the inhibition efficiency.

The charge transfer process of metal and bilayer behavior is related to the polarization resistance and bilayer capacitance.[58] This is an indication that the adsorption of coffee extract molecules can reduce surface inhomogeneity. In these cases, representing double-layer capacitors with a constant phase element (CPE) allows for a more accurate fit to the experimental data set.

The use of CPE instead of an ideal capacitor also agrees with the observed depressed semicircles. Furthermore, the increased absolute impedance of the Bode diagram at low-frequency values indicates that the shielding effect of the inhibitor increases with increasing the HECG concentration.[15] The phase angle plot shows that increasing the inhibitor concentration produces an absolute value close to 88°. This hints to a good contact between HECG molecules and the surface of S-steel at higher concentrations.[59]

The inset of Fig. 4a shows the corresponding equivalent electrical circuit that was used to model the experimental EIS data. In this circuit, R_s is the solution resistance, R_{ct} is the charge transfer resistance, CPE_{dl} represents the constant phase element associated with the electric double layer, R_f is the film resistance created by the corrosion product and oxide film, and CPE_f for the film capacitance. As well, CPE was used to consider surface inhomogeneity, inhibitor dislocations, grain boundaries, and passive layer formation.[60]

The CPE can be expressed as follows [61]

$$Z_{CPE} = \frac{(j\omega)^{-n}}{Q} \quad (18)$$

where, Q represents the pseudo-capacitance, and is influenced by the angular frequency ω (in rad s^{-1}), the imaginary unit $j^2 = -1$, and the CPE exponent n. The value of n determines the behavior of the CPE: it acts as an ideal resistor when $n = 0$ and as a perfect capacitor when $n = 1$. Moreover, n serves as a physical parameter that reflects intermediate phase characteristics, such as the surface roughness and the inhibitory adsorption properties of the working electrode. Table 4 summarizes the electrochemical parameters obtained by fitting the EIS data to the electrical circuit shown in Fig. 4 for different concentrations of HECG in SWCO biodiesel.

Notably, from Table 4 it is clear that R_{ct} increases by increasing the HECG additive concentration, suggesting the hindered metal oxidation *via* the formation of a physical barrier

Table 4 EIS fitting parameters for 307 L S-steel in SWCO biodiesel with various HECG concentrations

Conc. (ppm)	R_s (kΩ cm²)	Q_{dl} (μs^n Ω^{-1} cm^{-2})	n_{dl}	R_{ct} (kΩ cm²)	Q_f (μs^n Ω^{-1} cm^{-2})	n_f	R_f (kΩ cm²)	R_p (kΩ cm²)	η_{EIS} (%)
0	7.8 ± 0.7	0.082 ± 0.004	0.95 ± 0.03	7.4 ± 0.2	0.021 ± 0.001	0.90 ± 0.04	390 ± 40	397.4	—
500	9.9 ± 0.4	0.019 ± 0.001	0.91 ± 0.03	8.9 ± 0.3	0.10 ± 0.05	0.92 ± 0.04	1800 ± 200	1808.9	78.0
750	16.0 ± 2	0.016 ± 0.001	0.85 ± 0.03	22.0 ± 2	0.011 ± 0.001	0.87 ± 0.03	3100 ± 300	3122	87.3
1500	11.5 ± 0.6	0.013 ± 0.01	1.00 ± 0.03	380 ± 30	0.044 ± 0.002	0.98 ± 0.04	6000 ± 200	6380	93.8

on the surface. In addition, the charge transfer resistance R_{ct} of 307 LS-steel is higher than that of the film R_f. In contrast, the decrease in Q_{dl} could be due to a decrease in the local dielectric constant and/or an increase in the thickness of the electrical double layer. This implies that the metal's corrosion resistance is primarily due to the film formed during immersion.[62] The EIS results also show that as the HECG concentration increases, the η_{EIS} (%) improves steadily. In the case of 1500 ppm, a maximum value of 938% is achieved. For comparison with other reported studies on natural extracts as inhibitors in biodiesel, cardanol extract from cashew nutshell liquid showed improved inhibition efficiency (93.2%) for Al surface in soybean biofuel.[25] Recently, *Thymus vulgaris* extract showed a significant decrease in aluminum corrosion in 20% biodiesel-80% diesel blend.[27] *Syzygium aromaticum* flower extract revealed a maximum copper corrosion protection of 97.9% in neem biodiesel, however this result was obtained by a simple estimation using weight loss measurements.[63] Additionally, *Terminalia catappa* leaf extract also showed a reduction of corrosion of carbon steel and zinc, however its corrosion inhibition efficiency was limited (78% at room temperature and 8% at 60 °C for zinc).[26] The better or at least comparable inhibition efficiency of our coffee bean ground extract compared to reported studies suggests that this HECG extract has the potential for corrosion protection in soybean biodiesel.

3.4.3. Temperature effect and thermodynamic parameters. The environment and its temperature are the primary factors influencing the corrosion phenomenon. Therefore, polarization experiments were performed in the temperature range of 298–350 K in the absence and presence of the inhibitor at its optimum concentration (1500 ppm) as indicated in Fig. 5a, b and Table 5 lists the corresponding electrochemical parameters. Under both inhibitory and non-inhibitory conditions, the corrosion rate of 307 L S-steel increases with temperature. Based on the data, it is noticeable that the i_{corr} values in the presence of HECG increase moderately with rising the temperature, while in the biodiesel medium a significant increase was recorded.[64] Furthermore, a slight decrease in inhibition efficiency to 73.6% at 350 K indicates that the inhibitor molecules are still functioning on the metal surface and active in the studied temperature range. The decrease in the protection efficiency at elevated temperatures is possibly due to the increased mobility of the inhibitor and partial detachment from the electrode surface.

Table 5 Electrochemical parameters obtained from the polarization curves at 307 L S-steel in the absence and presence of 1500 ppm HECG at different temperatures 298–350 K

Solution	T (K)	$-E_{corr}$ (mV *vs.* SCE)	i_{corr} (nA cm^{-2})	η_{PDP}%
Blank	298	154	206	—
	308	105	347	—
	318	118	817	—
	328	138	948	—
	350	175	1340	—
1500 ppm HECG	298	180	13	93.7
	308	147	57	83.6
	318	221	163	80.1
	328	180	216	77.2
	350	134	355	73.6

The activation energies (E_a), enthalpies (ΔH_a), and activation entropies (ΔS_a) are important to gain insights into the mechanism of HECG inhibition. Using Arrhenius eqn (19), one can determine E_a from the slope of the plot of ln(i_{corr}) as a function of (1000/T) at different temperatures (Fig. 6a) according to the following eqn:

$$i_{corr} = A\exp\left(\frac{-E_a}{RT}\right) \quad (19)$$

whereby, N_A is Avogadro's number, h is the Planck constant, ΔH_a and ΔS_a are the activation enthalpy and activation entropy, respectively. Furthermore, the following eqn (20). Was used to determine the enthalpy and entropy. A straight line is obtained by plotting ln(i_{corr})/T as a function of (1000/T) (Fig. 6b); its slope is ($-\Delta H_a/R$) and its intersection with the ln(i_{corr})/T axis gives the parameter ΔS_a.

$$i_{corr} = \frac{RT}{Nh}\exp\left(\frac{\Delta S_a}{T}\right)\exp\left(\frac{-\Delta H_a}{RT}\right) \quad (20)$$

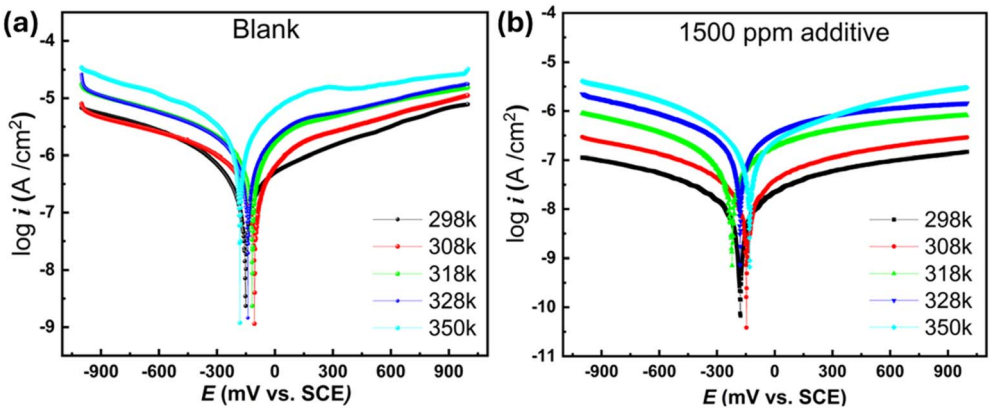

Fig. 5 Potentiodynamic polarization curves for 307 L S-steel in SWCO biodiesel without (a) and with (b) the addition of 1500 ppm of HECG at various temperatures (298–350).

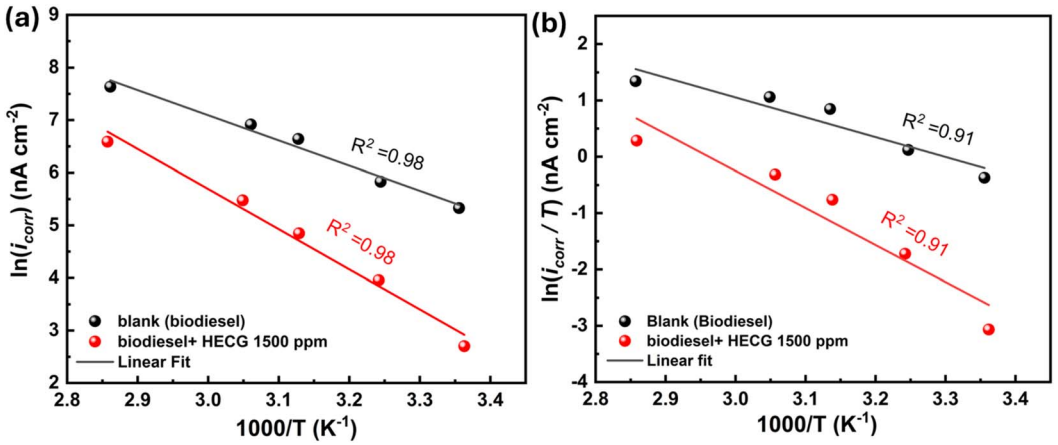

Fig. 6 (a) Arrhenius plots of ln(i_{corr}) *versus* 1/T and (b) Arrhenius plot of ln(i_{corr}/T) *versus* 1/T for 307 L S-steel with and without HECG additive at the optimal concentration of 1500 ppm and various temperatures.

with E_a representing the corrosion activation energy, R denoting the universal gas constant, T representing the absolute temperature, and A corresponding to the pre-exponential Arrhenius factor. E_a values of 31.8 and 52.9 kJ mol^{-1} were obtained for the blank and inhibited solutions, respectively.

As indicated in Table 6 indicates, the higher values of E_a in the presence of HECG is a clear indication of the high inhibitory effect of the HECG by enhancing the corrosion process's energetic level. This may also be related to the increase in the double-layer thickness, which improves the E_a of the corrosion process.[65] The increase in E_a reveals the presence of electrostatic connections between the inhibitor molecules and the steel surface, raising the energy barrier for corrosion.[66] The activation enthalpy ΔH_a values, which are positive for both the blank and the additive, indicate that the corrosion process is endothermic. Moreover, the higher ΔS_a value in the inhibited system compared to the uninhibited system suggests an increase in disorder accompanying the transition from the reactant state to the activated complex. This observation highlights the critical role of the concentration of the additive HECG in facilitating its adsorption onto the 307 L stainless steel surface by overcoming the energy barriers. The resulting increase in ΔS_a to less negative values reflects the enhanced disruption of the system's structural organization, consistent with the inhibitor's effectiveness.[67] It is worth noting that although many studies have used simple adsorption isotherms to predict adsorption mechanisms of extracts, modeling adsorption data with simple isotherms for multi-component extracts as in our work it isn't suitable to describe such a complex adsorption case and can be misleading when calculating adsorption coefficients. Thus, it hasn't been considered in this study.

3.5. UV-Vis-NIR spectroscopy analysis of the effect of the additive

The characteristics of the corrosion products formed on the surface of 307 L S-steel after immersion in SWCO biodiesel for 1128 h in the presence and absence of HECG at 37 °C were characterized using UV-Vis-NIR analysis, as shown in Fig. 7. The UV-Vis-NIR spectra were analyzed with the 2D derivative using the Savitzky–Golay function to reveal the weak peaks and avoid the baseline effects. A minimum in the second derivative curve represents the position of an absorption band. The curves were split into two regions (lower wavelength region in Fig. 7a and higher wavelength region in Fig. 7b. Moreover, by pinpointing the sensitive absorption bands in the second derivatives of the absorption curve, it was feasible to follow the changes in the bands that might result from electronic or vibrational transitions in the corrosion products.

The spectra of 307 L S-steel showed similar features and peaks in the presence and absence of the HECG inhibitor, with only the peaks becoming more intense in the longer wavelength range in the inhibited case. The surface of 307 L S-steel showed peaks that can be assigned to iron and chromium oxides as the main products at the surface, in agreement with previous reports.[68] For example, the observed peaks at 214 and 252 nm can be assigned to the electronic transitions of lepidocrocite (γ-FeOOH) and maghemite (γ-Fe_2O_3), respectively. Furthermore, the observed absorption bands between 300 nm and 900 nm in the spectra can be attributed to other types of iron oxides and chromium oxides (Cr_2O_3, CrOOH).[69,70] Moreover, there is a slight change in the amplitude of the iron and chromium oxide peaks between the solution with 1500 ppm inhibitor and that without inhibitor. This could indicate that the inhibitor

Table 6 Thermodynamic parameters obtained for 307 L S-steel in SWCO biodiesel with and without HECG

Medium	E_a (kJ mol^{-1})	ΔH_a (kJ mol^{-1})	$E_a - \Delta H_a$ (kJ mol^{-1})	ΔS_a (J mol^{-1} K^{-1})
Blank	31.8	29.1	2.7	−101.5
HECG additive	52.9	50.2	2.7	−50.3

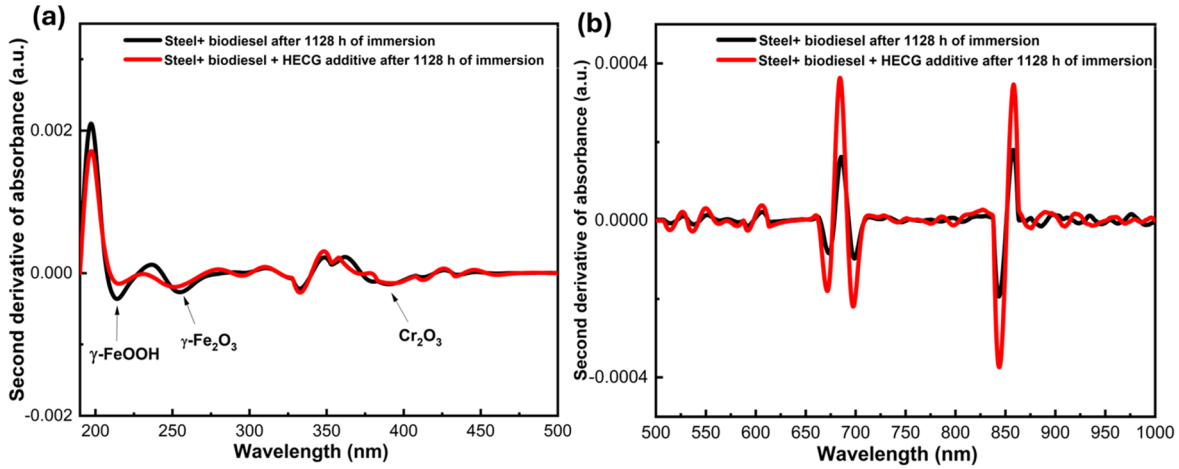

Fig. 7 UV-Vis-NIR spectra represented in the second derivative of the Savitzky–Golay SWCO biodiesel for 1128 h in the presence and absence of HECG at 37 °C, (a) in the range of 190–500 nm, and (b) 500–1000 nm.

promotes the formation of a passive oxide layer on the metal surface, which effectively protects it from damage and thus achieves a considerable protective effect.

3.6. UV-vis absorption spectroscopy

The inhibitory effect of HECG was further evaluated using UV-vis spectroscopy. Fig. S2 depicts the UV-Vis spectra of the SWCO biodiesel (black line) after immersion 307 L S-steel for 1128 h at 37 °C and in the same solution after the addition of 1500 ppm HECG additive (red line). The data in Fig. S2 reveals that the blank biodiesel sample shows an absorption peak at 224 nm, which can be attributed to the presence of dissolved metal ions or organic degradation products resulting from the corrosion of 307 L S-steel. Upon the addition of the HECG inhibitor, this peak is shifted to 244 nm with increased intensity, suggesting the formation of complexes between the inhibitor molecules and metal ions, thereby altering the electronic environment.[71] This spectral shift in UV-Vis spectra implies that the HECG inhibitor interacts with the corrosion byproducts, potentially forming a protective layer on the steel surface, which reduces metal dissolution and modifies the absorption characteristics.

For instance, the oxidation of polyunsaturated fatty acids (PUFAs) in biodiesel can lead to the formation of conjugated double bonds, enhancing its anticorrosion properties. Adding HECG to SWCO biodiesel promotes this oxidative transformation, which is beneficial for raising the corrosion resistance. Moreover, conjugated double bonds possess electron-rich structures that can interact with metal surfaces, forming protective layers that reduce corrosion rates. This interaction is particularly beneficial in biodiesel applications, where the presence of unsaturated bonds in fatty acids contributes to the overall inhibition efficiency. It has been reported that the oxidation-induced conjugation of linoleic acid's double bonds in SWCO biodiesel, facilitated by HECG, may improve its corrosion inhibition properties, offering a promising approach to prolong the lifespan of metal components in biodiesel systems.[72] Such findings underscore the efficacy of HECG as a corrosion inhibitor in biodiesel environments, highlighting its role in mitigating corrosion processes and enhancing the oxidative stability of biodiesel during storage.

3.7. Microstructure imaging using SEM-EDX

The surface morphology of the 307 L S-steel investigated for polished, uninhibited, and exposed surfaces inhibited in biodiesel after 1128 h of immersion was characterized using SEM-EDX. The morphology of the polished specimen is shown in the SEM image in Fig. 8a, which also amply demonstrates the scratches left behind by manual polishing. The SEM image in Fig. 8b for the surface after immersion in only biodiesel demonstrates some changes such as scratches, some dark spots and surface damage in the exposed surface of the 307 L S-steel by the acid molecules present in the SWCO biodiesel. After the addition of HECG in the biodiesel, the steel surface showed the formation of some deposits and a layer that covers the underlying original scratches, as shown in Fig. 8c.

To represent the distribution of film formation formed on the surface of S-steel, EDX spectra were recorded (See Fig. S3). By comparing the C content from the EDX analysis of the pristine polished 307 L S-steel (Fig. S3a) with that of 307 L S-steel immersed in SWCO biodiesel (Fig. S3), it is clearly observed that the C content has significantly increased, suggesting that an organic deposit is accumulated on its surface. Corrosion products probably absorb and adhere when the metal reacts with many unsaturated fatty acids, adding more carbon and oxygen to the surface. The EDX spectrum in Fig. S3c reveals the presence of a small nitrogen peak, a characteristic element of the organic molecules of the inhibitor, alongside carbon and oxygen peaks. This may hint to the formation of a layer on the 307 L S-steel surface, suggesting the adsorption of the inhibitor molecules.[73] In addition, stainless steel elements such as Fe and Cr were also identified whose signals were reduced on the inhibited surface compared to the polished surface and increased compared to the non-inhibited surface, indicating the presence of HECG on the surface.[74]

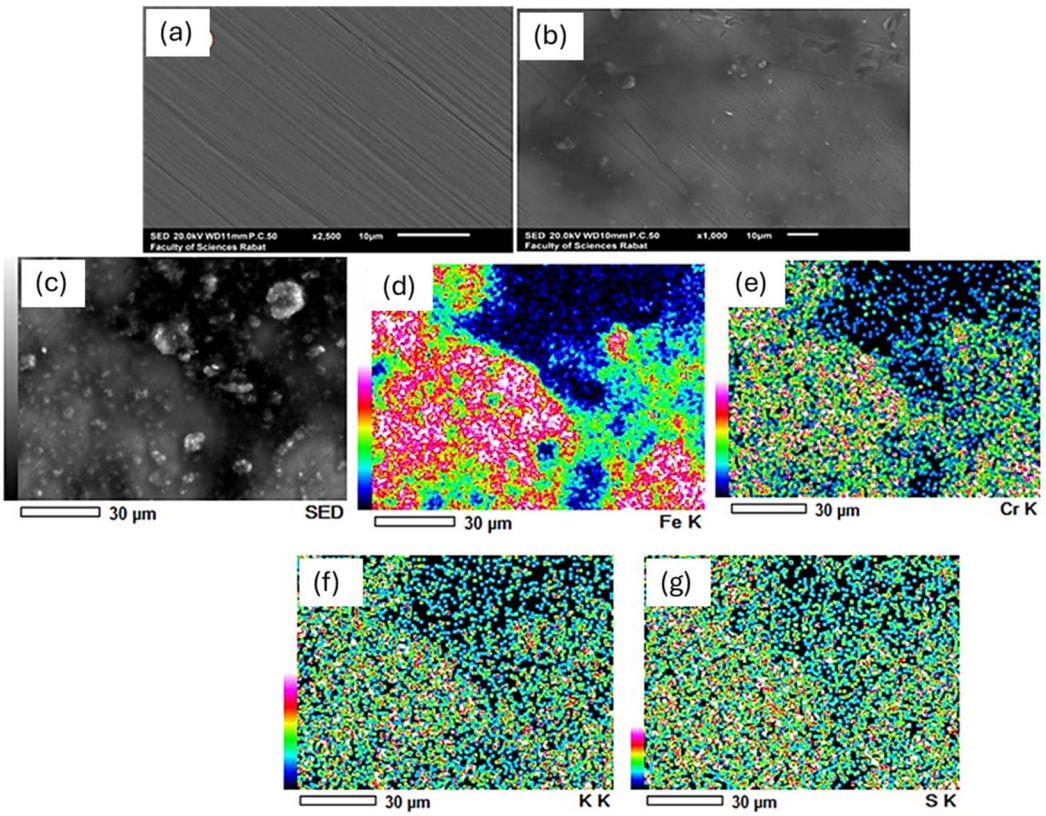

Fig. 8 SEM images for the polished (a) and uninhibited (b) and inhibited (c) electrode exposed to SWCO biodiesel after 1128 h of immersion. (d–g) EDX mapping of Fe, Cr, K and S elements for the inhibited electrode.

3.8. XRD analysis

Due to the possibility of interaction between 307 L S-steel and the corrosive environment under various circumstances, forming passive oxides or corrosion products, XRD was used to characterize the crystal structure of the surface.

As illustrated in Fig. 9, the components that contribute to protection of the steel against corrosion are Fe_2O_3 and Cr_2O_3, which are the dominant oxide responsible for its high corrosion resistance in the absence and presence of HECG, with intensities increasing after the addition of the inhibitor.[75]

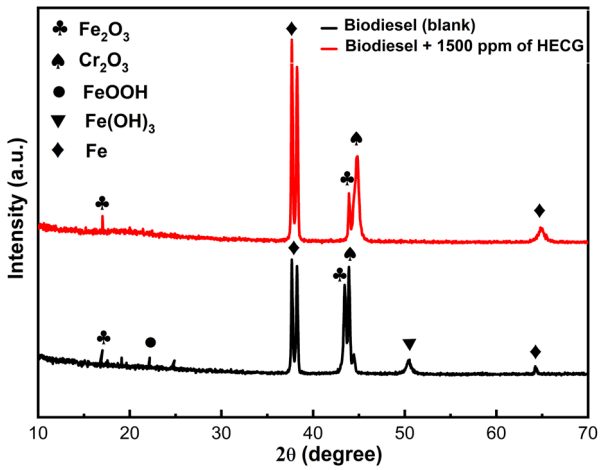

Fig. 9 XRD patterns of the formed corrosion products on the 307 L S-steel surface after 1128 hours of immersion in the optimal inhibitor concentration and blank SWCO biodiesel.

Similarly, the appearance of peaks corresponding to non-protective corrosion compounds $Fe(OH)_3$ and FeOOH in the biodiesel was observed. The oxygenation of biodiesel can enhance the 307 L S-steel corrosion additionally.[76] It has been reported that biodiesel's resistance towards oxygenation is related to its fatty constituents, which disappear after the addition of HECG, suggesting its effectiveness in blocking the dissolution of the metal by retreading the corrosion rate.[77] We note that XRD is still not a very sensitive surface technique but rather gives hints to the nature of the metal surface.

3.9. DFT calculation and Fukui functions: mechanistic insights

DFT is a powerful computational tool widely used in corrosion studies to understand the mechanisms at the atomic and molecular levels. In this study, DFT is used to model how β-turmerone, the major component of the spent coffee grounds extract, interacts with the stainless-steel surface, potentially forming a protective layer or altering the oxidation process, thus enhancing the material's corrosion resistance.

Fig. 10 shows the frontier molecular orbitals (FMO) of the β-turmerone molecule. Considering the HOMO surface, the wavefunctions are mostly located at the double bonds over the

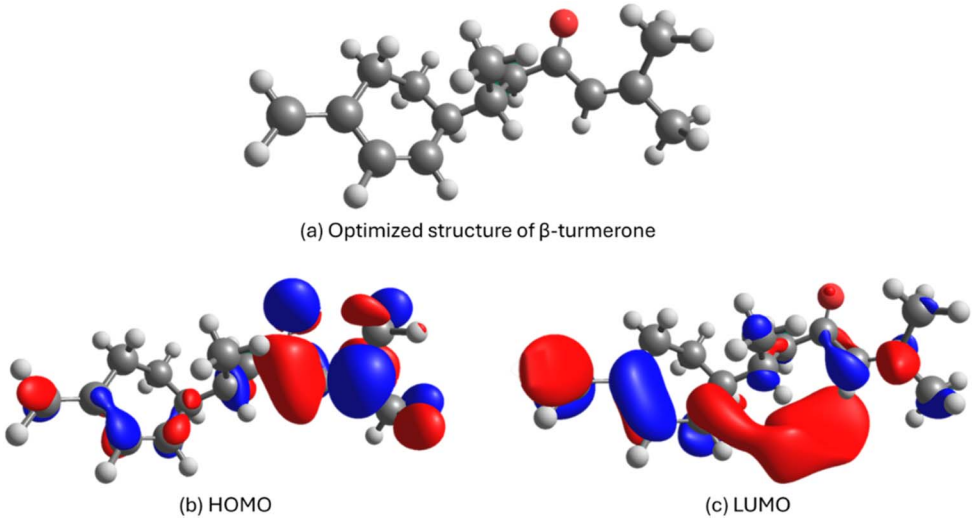

Fig. 10 The optimized structure of β-turmerone (a), and the HOMO (b) and LUMO (c) calculated structures.

carbonyl and isopropenyl group, which is consistent with the sp^2 hybridization having a π bonding. Additionally, in the cyclohexane ring, there is a small number of HOMO surfaces once there are non-bonding electrons in those structures. The isopropenyl group is conjugated with the carbonyl group of β-turmerone, which explains the high concentration of HOMO on those groups. On the other hand, the LUMO surfaces are located mostly outside of the β-turmerone molecule. Since the β-turmerone has many sp^2 bonds, the molecular geometry favors the superposition of the unoccupied orbitals, and a lobe (at least, one of them) is not located into the molecule. However, the LUMO lobe that is outside the molecule connects with the LUMO from carbon atoms of the cyclohexenyl ring, showing that this LUMO lobe isn't completely unbonded from the molecule. Furthermore, the cyclohexane ring presents a visible π–π bonding with the expected superposition of the wavefunctions of this kind of bond along with sole p-orbital of the carbon in the methylene group. In the rest of the molecule, the conjugated sp^2–sp^3 bonds from carbonyl towards isopropenyl groups are also shown but in lower quantities than the HOMO surfaces discussed above. Those FMOs over the β-turmerone molecule drive the possibility of having some types of organic reactions, as shown in Fukui's analysis of the β-turmerone, discussed below. Table 7 summarizes important molecular descriptors that are obtained from FMO data for the β-turmerone molecule.

The molecular descriptors for β-turmerone shown in Table 7 demonstrate that the molecule tends to donate charge density towards the steel electrode. This can be supported by the ΔN value, which is 1.314 and lower than 3.6, the value reported by Lukovits *et al.*.[45] ΔN reflects the tendency of electronic density flow towards the electrode. A value lower than 3.6 suggests that the molecule has a great tendency to transfer its electrons to the metal. The discussed FMO above explains why this occurs since the HOMO orbitals are concentrated over the carbonyl and isopropenyl groups of the β-turmerone molecule. On the other hand, the LUMO lobe has mostly erupted from the molecule, and a retrodonation bonding between the β-turmerone and steel surface can be thought of. The liquid electrophilicity ($\Delta\omega$) showed a negative value, suggesting that the tendency for the β-turmerone molecule to donate electrons toward the steel electrode. Therefore, the FMO analysis shows that the β-turmerone adsorbs onto the steel surface and thus protects it from oxidization.

Table 7 Molecular descriptors obtained from DFT calculation for the optimized β-turmerone structure

IE (eV)	EA (eV)	ω^+ (eV)	ω^- (eV)	$\Delta\omega$ (eV)	ΔN
7.567	0.438	0.691	4.694	−4.003	1.314

Fig. 11 displays the Fukui function surfaces for a β-turmerone molecule. Considering the nucleophilic reactions (Fig. 11a), the wavefunctions are located between the carbonyl and isopropenyl conjugated bonds, while the other side of the molecule is dominated by an electrophilic wavefunction, Fig. 11b, which has the cyclohexenyl ring with a methylene group. The location of those wavefunctions corresponds to the organic chemistry theory of those reactions. Considering the anticorrosion behavior of β-turmerone from the perspective of the Fukui theory, the discussion is complementary to the FMO discussion. The electrophilic surface found at the β-turmerone molecule implies that electrons can be transferred from the steel electrode surface, whilst the nucleophilic surface indicates that the molecule donates electrons towards the steel electrode, making a coordination compound and thus allows retrodonations in both ways, *i.e.* molecule-to-electrode and/or electrode-to-molecule. Considering the antioxidation properties of the β-turmerone in solution, the radical wavefunctions are mostly located at the cyclohexenyl with the bonded methylene group, which can undergo a radical reaction and neutralize an oxidant species in biodiesel.

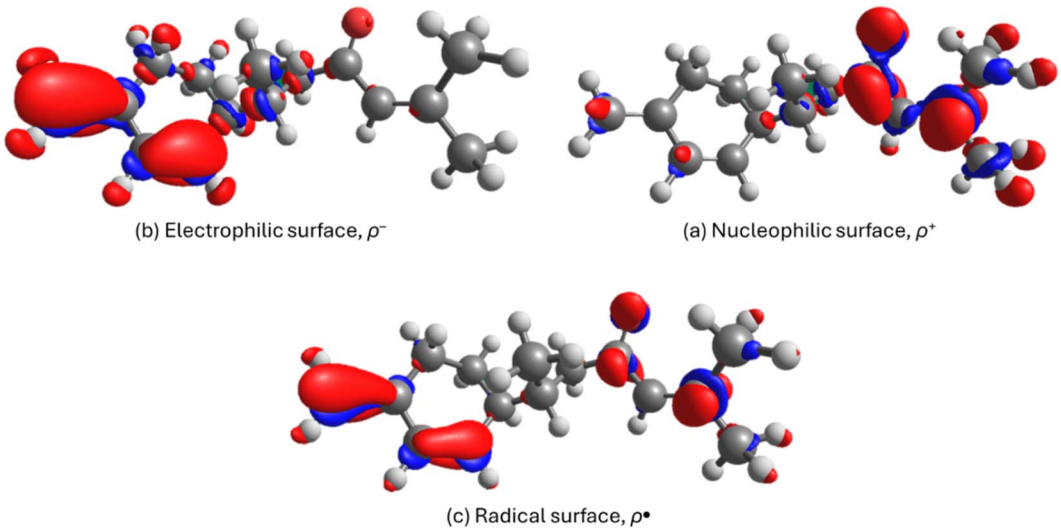

Fig. 11 Surface Fukui functions for nucleophilic (a), electrophilic (b), and radical (c) reactions at β-turmerone molecules.

4. Conclusions

The results demonstrated the promising recycling potential of spent coffee ground extract as a green additive in soybean cooking oil biofuel, improving its corrosive effects on 307 L stainless steel. HECG revealed an optimal protection efficiency of 93.5% using 1500 ppm coffee extract additive at room temperature (298 K). This improved efficiency, confirmed through weight loss assessments, electrochemical techniques, and surface analysis, results from HECG's ability to obstruct active corrosion sites, though its performance decreases with rising temperatures due to steel dissolution. Potentiodynamic polarization identified HECG as a mixed-type inhibitor, while EIS results indicated a reduction in charge transfer resistance, suggesting the formation of a protective film on the steel surface. SEM and XRD analyses further validated the inhibitor's effectiveness. Similarly, DFT simulations on β-turmerone, the major extract component, highlighted reactive regions that contribute to their anticorrosion properties, enhancing biodiesel viability. The HOMO is concentrated around the carbonyl and isopropenyl groups, while the partially external LUMO allows for organic reactivity, supported by Fukui function analysis that identifies nucleophilic and electrophilic zones aligned with anticorrosion behavior. Together, these findings on HECG underscore its promise in protecting metals and enhancing biodiesel sustainability through their distinctive chemical reactivities and protective mechanisms.

Author contributions

M. El Hawary: methodology, investigation, writing – original draft. M. Boudalia: methodology, data curation, validation, supervision, writing – review & editing. O. S. Campos: simulation, writing – original draft. Y. Kerroum: writing – review & editing, data curation. A. Bellaouchou: resources, project administration, supervision. H. M. A. Amin: conceptualization, data curation, visualization, writing – review & editing. All authors have read and agreed to the published version of the manuscript.

Conflicts of interest

The authors declare no competing interests.

Data availability

The authors confirm that the data supporting the findings of this study are available within the article and its SI file.

Supplementary information: Details of sample collection, extraction, synthesis and physicochemical characterizations; table of physicochemical parameters of the soybean biodiesel; GC-MS of extract; UV-Vis absorption spectra of the SWCO biodiesel before and after immersion of steel; EDX spectra of 307L S-steel before and after immersion in studies solutions. See DOI: **https://doi.org/10.1039/d5ra04888e**.

References

1 D. Singh, D. Sharma, S. L. Soni, C. S. Inda, S. Sharma, P. K. Sharma and A. Jhalani, *J. Clean. Prod.*, 2021, **307**, 127299.
2 O. Awogbemi and D. V. Von Kallon, *Heliyon*, 2022, **8**, e11117.
3 S. B. Monika and V. V Pathak, *Energy Nexus*, 2023, **10**, 100209.
4 L. Rocha-Meneses, A. Hari, A. Inayat, L. A. Yousef, S. Alarab, M. Abdallah, A. Shanableh, C. Ghenai, S. Shanmugam and T. Kikas, *Fuel*, 2023, **348**, 128514.
5 M. U. H. Suzihaque, H. Alwi, U. Kalthum Ibrahim, S. Abdullah and N. Haron, *Mater. Today Proc.*, 2022, **63**, S490–S495.
6 Y. Zhang, Y. Zhong, S. Lu, Z. Zhang and D. Tan, *Processes*, 2022, **10**, 1178.

7 M. A. Fazal, A. S. M. A. Haseeb and H. H. Masjuki, *Fuel Process. Technol.*, 2010, **91**, 1308–1315.
8 X. Lu, *Cem. Concr. Res.*, 1997, **27**, 293–302.
9 B. Singh, J. Korstad and Y. C. Sharma, *Renew. Sustain. Energy Rev.*, 2012, **16**, 3401–3408.
10 X. P. Nguyen and H. N. Vu, *Int. J. Renew. Energy Dev.*, 2019, **8**, 119–132.
11 A. S. M. A. Haseeb, M. A. Fazal, M. I. Jahirul and H. H. Masjuki, *Fuel*, 2011, **90**, 922–931.
12 C. I. Rocabruno-Valdés, *Int. J. Electrochem. Sci.*, 2020, **15**, 334–349.
13 J. R. Davis, in *Corrosion: Understanding the Basics*, ASM International, 2000, pp. 1–20.
14 M. Boudalia, M. Laourayed, M. El Moudane, Z. Sekkat, O. S. Campos, A. Bellaouchou, A. Guenbour, A. José Garcia and H. M. A. Amin, *J. Alloys Compd.*, 2023, **938**, 168570.
15 H. Amegroud, M. Boudalia, M. Elhawary, A. J. Garcia, A. Bellaouchou and H. M. A. Amin, *Colloids Surf., A*, 2024, **691**, 133909.
16 A. Boutoumit, M. Elhawary, A. Bellaouchou, M. Boudalia, O. Hammani, A. José Garcia and H. M. A. Amin, *Coatings*, 2024, **14**, 783.
17 M. M. Solomon, S. A. Umoren, A. Gilda Ritacca, I. Ritacco, D. Hu and L. Guo, *J. Mol. Liq.*, 2024, **396**, 123935.
18 T.-R. Ovari, T. Toth, G. Katona, G. S. Szabó and L. M. Muresan, *Coatings*, 2023, **13**, 1844.
19 Z. Zhang, Z.-Y. Liu, R.-Z. Zhang, H.-Q. Liu and Y. Gu, *J. Alloys Compd.*, 2023, **966**, 171552.
20 A. Najem, O. S. Campos, G. Girst, M. Raji, A. Hunyadi, J. García-Antón, A. Bellaouchou, H. M. A. Amin and M. Boudalia, *J. Electrochem. Soc.*, 2023, **170**, 093512.
21 H. M. A. Amin and A. Galal, *Corrosion Protection of Metals and Alloys Using Graphene and Biopolymer Based Nanocomposites*, CRC Press is an imprint of Taylor, Boca Raton, 1st edn, 2021.
22 T. Peme, L. O. Olasunkanmi, I. Bahadur, A. S. Adekunle, M. M. Kabanda and E. E. Ebenso, *Molecules*, 2015, **20**, 16004–16029.
23 B. E. A. Rani and B. B. J. Basu, *Int. J. Corros.*, 2012, **2012**, 1–15.
24 G. Salinas-Solano, J. Porcayo-Calderon, L. M. Martinez de la Escalera, J. Canto, M. Casales-Diaz, O. Sotelo-Mazon, J. Henao and L. Martinez-Gomez, *Ind. Crops Prod.*, 2018, **119**, 111–124.
25 M. A. Deyab, R. G. C. Corrêa, S. E. Mazzetto, A. S. Dhmees and G. Mele, *Ind. Crops Prod.*, 2019, **130**, 146–150.
26 F. D. Fernandes, L. M. Ferreira and M. L. C. P. da Silva, *J. Clean. Prod.*, 2021, **321**, 128863.
27 D. A. Nogueron Benitez, A. K. Larios Galvez, R. Lopez Sesenes, A. M. Ramirez Arteaga and J. G. Gonzalez Rodriguez, *Green Chem. Lett. Rev.*, 2025, **18**, 2525085.
28 A. Nayak and B. Bhushan, *J. Environ. Manage.*, 2019, **233**, 352–370.
29 G. Rouin, M. Abdelmouleh, A. Mallah and M. Masmoudi, *Coatings*, 2023, **13**, 1745.
30 M. A. J. L. Da Costa, J. S. De Gois, I. M. Toaldo, A. C. F. Bauerfeldt, D. B. Batista, M. T. Bordignon-Luiz, D. C. B. Do Lago, A. S. Luna and L. F. De Senna, *Mater. Res.*, 2020, **23**, 1–12.
31 M. El Hawary, M. Khachani, G. Kaichouh, A. Guenbour, A. Zarrouk and A. Bellaouchou, *J. Bio Tribo Corros.*, 2021, **7**, 1–13.
32 T. Tsoutsos, S. Tournaki, Z. Gkouskos, O. Paraíba, F. Giglio, P. Q. García, J. Braga, H. Adrianos and M. Filice, *ChemEngineering*, 2019, **3**, 1–13.
33 F. Anguebes-Franseschi, A. Bassam, M. Abatal, O. May Tzuc, C. Aguilar-Ucán, A. T. Wakida-Kusunoki, S. E. Diaz-Mendez and L. C. San Pedro, *J. Chem.*, 2019, **2019**, 1–12.
34 ASTM, *Standard Practice for Laboratory Immersion Corrosion Testing of Metals*, ASTM G31-72, ASTM International, 2004, DOI: **10.1520/G0031-72R04**.
35 M. D. Hanwell, D. E. Curtis, D. C. Lonie, T. Vandermeersch, E. Zurek and G. R. Hutchison, *J. Cheminform.*, 2012, **4**, 17.
36 C. Bannwarth, S. Ehlert and S. Grimme, *J. Chem. Theory Comput.*, 2019, **15**, 1652–1671.
37 F. Neese, *Wiley Interdiscip. Rev. Comput. Mol. Sci.*, 2022, **12**, e1606.
38 Y. Zhao and D. G. Truhlar, *Theor. Chem. Acc.*, 2008, **120**, 215–241.
39 R. Krishnan, J. S. Binkley, R. Seeger and J. A. Pople, *J. Chem. Phys.*, 1980, **72**, 650–654.
40 W. F. Polik and J. R. Schmidt, *Wiley Interdiscip. Rev. Comput. Mol. Sci.*, 2022, **12**, 1–22.
41 N. V. P. Rangel, L. P. da Silva, V. S. Pinheiro, I. M. Figueredo, O. S. Campos, S. N. Costa, F. M. T. Luna, C. L. Cavalcante Jr, E. S. Marinho, P. de Lima-Neto and M. A. S. Rios, *Fuel*, 2021, **289**, 119939.
42 W. Yang and R. G. Parr, *Proc. Natl. Acad. Sci. U. S. A.*, 1985, **82**, 6723–6726.
43 R. G. Pearson, *Surv. Prog. Chem.*, 1969, **5**, 1–52.
44 R. G. Pearson, *J. Chem. Sci.*, 2005, **117**, 369–377.
45 I. B. Obot, D. D. Macdonald and Z. M. Gasem, *Corros. Sci.*, 2015, **99**, 1–30.
46 H. Chermette, *Coord. Chem. Rev.*, 1998, **178–180**, 699–721.
47 R. Pucci and G. G. N. Angilella, *Found. Chem.*, 2022, **24**, 59–71.
48 I. Barabas and I.-A. Todoru, in *Biodiesel- Quality, Emissions and By-Products*, InTech, 2011.
49 P. Verma and M. P. Sharma, *Renew. Sustain. Energy Rev.*, 2016, **62**, 1063–1071.
50 A. Panusa, A. Zuorro, R. Lavecchia, G. Marrosu and R. Petrucci, *J. Agric. Food Chem.*, 2013, **61**, 4162–4168.
51 J. P. Silva, G. L. Mendez, J. Lombana, D. G. Marrugo and R. Correa-Turizo, *Adv. J. Food Sci. Technol.*, 2018, **16**, 220–225.
52 J. Simões, É. Maricato, F. M. Nunes, M. R. Domingues and M. A. Coimbra, *Carbohydr. Polym.*, 2014, **101**, 256–264.
53 U. Eugene, P. S. O rsquo Donnell, V. J. Ifeoma and V. A. Feyisayo, *Afr. J. Pure Appl. Chem.*, 2016, **10**, 23–32.
54 N. Timoudan, A. S. Al-Gorair, L. El Foujji, I. Warad, Z. Safi, B. Dikici, F. Benhiba, A. E. K. Qaiss, R. Bouhfid, F. Bentiss, S. S. Al-Juaid, M. Abdallah and A. Zarrouk, *RSC Adv.*, 2024, **14**, 30295–30316.
55 M. Scendo and J. Trela, *Int. J. Electrochem. Sci.*, 2013, **8**, 9201–9221.

56 N. F. Atta, A. Galal and H. M. A. Amin, *Int. J. Electrochem. Sci.*, 2012, **7**, 3610–3626.
57 F. Z. Eddahhaoui, A. Najem, M. Elhawary, M. Boudalia, O. S. Campos, M. Tabyaoui, A. José Garcia, A. Bellaouchou and H. M. A. Amin, *J. Alloys Compd.*, 2024, **977**, 173307.
58 A. C. Lazanas and M. I. Prodromidis, *ACS Meas. Sci. Au*, 2023, **3**, 162–193.
59 A. S. Fouda, M. A. Migahed, A. A. Atia and I. M. Mousa, *J. Bio-Tribo-Corrosion*, 2016, **2**, 22.
60 M. R. Jakeria, M. A. Fazal and A. S. M. A. Haseeb, *Corros. Eng. Sci. Technol.*, 2015, **50**, 56–62.
61 H. Ashassi-Sorkhabi, D. Seifzadeh and M. G. Hosseini, *Corros. Sci.*, 2008, **50**, 3363–3370.
62 R. Naderi, A. Bautista, F. Velasco, M. Soleimani and M. Pourfath, *J. Mol. Liq.*, 2022, **346**, 117856.
63 S. Iyyappan, K. P. Vinod Kumar, P. Ponram and B. Karthik, *Ind. Crops Prod.*, 2024, **219**, 119073.
64 M. A. Deyab, *J. Taiwan Inst. Chem. Eng.*, 2016, **58**, 536–541.
65 A. Hamdy and N. S. El-Gendy, *Egypt. J. Pet.*, 2013, **22**, 17–25.
66 A. A. Khadom, A. S. Yaro, A. S. Altaie and A. A. H. Kadum, *Port. Electrochim. Acta*, 2009, **27**, 699–712.
67 M. Behpour, S. M. Ghoreishi, M. Khayatkashani and N. Soltani, *Corros. Sci.*, 2011, **53**, 2489–2501.
68 R. Guillamet, M. Lenglet and F. Adam, *Solid State Commun.*, 1992, **81**, 633–637.
69 A. C. Scheinost, A. Chavernas, V. Barrón and J. Torrent, *Clays Clay Miner.*, 1998, **46**, 528–536.
70 Y. Kerroum, A. Guenbour, A. Bellaouchou, H. Idrissi, J. García-Antón and A. Zarrouk, *Anal. Bioanal. Electrochem.*, 2019, **11**, 497–509.
71 F. H. N. Souza, L. R. De Almeida, F. Samuel, C. L. Batista and M. Alexsandra, *Energy Sci. Technol.*, 2011, **2**, 56–61.
72 A. Demirbas, *Energy Explor. Exploit.*, 2007, **25**, 63–70.
73 Z. Ai, J. Jiang, W. Sun, X. Jiang, B. Yu, K. Wang, Z. Zhang, D. Song, H. Ma and J. Zhang, *Cem. Concr. Compos.*, 2018, **92**, 178–187.
74 H. Wei, B. Heidarshenas, L. Zhou, G. Hussain, Q. Li and K. Ostrikov, *Mater. Today Sustain.*, 2020, **10**, 100044.
75 D. L. Cursaru, G. Brănoiu, I. Ramadan and F. Miculescu, *Ind. Crops Prod.*, 2014, **54**, 149–158.
76 M. S. Graboski and R. L. McCormick, *Prog. Energy Combust. Sci.*, 1998, **24**, 125–164.
77 B. R. Moser, F. J. Eller, B. H. Tisserat and A. Gravett, *Energy and Fuels*, 2011, **25**, 1869–1877.